

# Mimir: A Near-Infrared Wide-Field Imager, Spectrometer, and Polarimeter

D. P. CLEMENS, D. SARCIA, A. GRABAU, AND E. V. TOLLESTRUP<sup>1</sup>

Institute for Astrophysical Research, Boston University, Boston, MA; clemens@bu.edu; dsscryo@verizon.net; grabau@gmail.com; tolles@ifa.hawaii.edu;

AND

M. W. BUIE, E. DUNHAM, AND B. TAYLOR

Lowell Observatory, Flagstaff, AZ; buie@lowell.edu; dunham@lowell.edu; taylor@lowell.edu

Received 2007 September 12; accepted 2007 October 22; published 2007 December 21

**ABSTRACT.** Mimir, a new facility-class near-infrared instrument for the 1.8 m Perkins telescope on Anderson Mesa outside Flagstaff, Arizona, was commissioned and has been operating for three years. Mimir is multifunction, performing wide-field (F/5) and narrow-field (F/17) imaging, long-slit spectroscopy, and imaging polarimetry. The F/5 mode images at 0.59" per pixel onto the 1024 × 1024 pixel ALADDIN III InSb array detector, giving a 10' × 10' field of view. In the F/17 mode, the plate scale is 0.18" per pixel. Optically, Mimir is a refractive reimager for the F/17.5 Perkins beam. A six-lens collimator produces an achromatic 25 mm pupil, which is imaged by a five-lens camera (F/5), a four-lens camera (F/17), or a two-lens pupil viewer onto the detector. Three filter wheels precede the pupil, one follows the pupil. The wheels contain a rotating half-wave plate, broadband filters, narrowband filters, grisms, long-pass filters, a wire grid, and thermal IR blockers. The first telescope focus is within Mimir, where a slit and decker unit, consisting of two linear motion cars, selects one of 13 slit scenes. The slit and decker cars, the four filter wheels, the half-wave plate rotation, and the camera selector are all driven by stepper motors within the cold vacuum space. Cooling is provided by a CTI 1050 two-stage, closed-cycle helium refrigerator, keeping the optics, filters, and internal surfaces between 65 and 75 K and the detector at 33.5 K. Switching between Mimir's different modes takes only a few seconds, making it a versatile tool for conducting a wide range of investigations and for quickly reacting to changing observing conditions. Mimir on the Perkins telescope achieves imaging sensitivities 2–4 mag deeper than 2MASS, moderate resolution ( $R \sim 700$ ) *JHK* spectra of virtually any 2MASS source, high-precision wide-field imaging polarimetry, and  $L'$  and  $M'$  band imaging and spectroscopy.

## 1. INTRODUCTION

In 1999, Boston University became a partner with Lowell Observatory in the use of the 1.8 m Perkins telescope on Anderson Mesa, outside Flagstaff, Arizona. This initiated a project to develop a multifunction near-infrared (NIR) instrument to replace the OSIRIS (DePoy et al. 1993) NIR imager and spectrograph, which had until then been used on the Perkins telescope. Scientists from both institutions developed the high-level requirements for the new instrument, mostly driven by the need to monitor Pluto's NIR spectrum, to probe Galactic star formation regions, and to conduct wide-field imaging polarimetry for probing Galactic magnetic fields. The long focal length (F/17.5) telescope, its English equatorial mount, and the short distance to the dome floor levied additional design constraints.

Several other NIR imagers and spectrometers had been developed by then (e.g., CSHELL [Greene et al. 1993]; OSIRIS [DePoy et al. 1993]; NSFCAM [Shure et al. 1994]; Phoenix

[Hinkle et al. 1998]; STELIRCam [Tollestrup & Willner 1998]; NIRSPEC [McLean et al. 1998]) and several more were under development (FLAMINGOS [Elston 1998]; FLITECAM [Horn et al. 2000]; NIRI [Hodapp et al. 2003]; SPEX [Rayner et al. 2003]), but none of the existing designs could meet our science requirements or the available physical and cost envelopes. As a result, we designed, built, and have been operating a new instrument. Named "Mimir" after a Norse god, it meets the identified scientific needs as well as all of the telescope, operational, and budget constraints.

Mimir consists of a cooled refractive optical system, light analysis elements in rotating filter wheels, selectable refractive cameras, and an ALADDIN III InSb array detector, capable of efficiently detecting light from 0.6 to 5.5  $\mu\text{m}$  wavelength. Mimir draws some of its heritage from STELIRCam (Tollestrup & Willner 1998) and FLITECAM (Horn & McLean 2000; Horn et al. 2000), the first via one coauthor (E. T.) and the second from extensive discussions with J. Horn (private communication 2000). In the following sections, we present the optical designs and prescriptions, the mechanical design approach and some examples, an overview of the cryogenics system,

<sup>1</sup>Current address: NASA Infrared Telescope Facility, Institute for Astronomy, University of Hawaii, Hilo, HI.

an overview of the sensing and control systems, and a summary of the operating conditions of the array detector. These sections are followed by examples of Mimir data showing imaging, spectroscopy, and polarimetric properties.

## 2. REQUIREMENTS REVIEW

Top level science requirements for Mimir were developed from planetary and Galactic science drivers. In planetary science, these included synoptic spectroscopic observations of Pluto to determine the physical state of surface ices and temporal evolution (e.g., Grundy & Buie 2000, 2002; Grundy et al. 2003), Io volcanism, satellite occultations, and studies of the atmospheres of Jovian and terrestrial planets. Key drivers in Galactic science included young stellar clusters, photodissociation regions, the internal structures of dark molecular clouds, and large-area surveys of the Galactic magnetic field. These science goals demanded a flexible instrument meeting the requirements listed in Table 1. The closed-cycle helium refrigerator approach allows Mimir to remain cold for long periods of time with minimal or no intervention. This can be critical if a snow storm makes the telescope inaccessible.

## 3. OPTICAL DESIGN HIGHLIGHTS

The combination of astronomical, optical, and physical requirements listed in Table 1 led to selection of an unbent, refractive, reimager design. The design used ZEMAX-EE (ZEMAX Dev. Corp., Bellevue, Washington), assumed an instrument internal working environment of 70 K and vacuum, and included the Perkins telescope optics. To avoid mechanical interferences in warm, cold, or changing thermal conditions, a 1 mm minimum element spacing was enforced. The values for warm and cold refractive indices and coefficients of thermal expansion (CTE) were kindly provided by J. Rayner & H. Epps (private communication 2001) or were drawn from published works (e.g., Feldman et al. 1979). Prior to making detailed drawings, the parts were appropriately scaled to room temperature conditions.

The optics were fabricated and inspected by Lambda Research Optics (Costa Mesa, California) while the mechanical parts were made at the Boston University Scientific Instruments Facility.<sup>2</sup> After the optics were completed, spacings in the design were reoptimized based on the as-built lens data and final spacers were machined.

For design purposes, the optics were separated into four groups: collimator, F/5 camera, F/17 camera, and pupil viewer. The collimator and F/5 camera groups were designed first, with the simpler F/17 and pupil viewer groups done subsequently. Considerable effort went into reducing the lens count and material types. Iteration of the design was needed to meet image

quality requirements while maintaining reasonable tolerances. Similar iteration of the design was needed to control ghost reflections. Strongly saturated stars do produce out-of-focus ghosts, but these can be removed through dithered observations.

The final optical design prescriptions are listed in Table 2 and the optical layout is shown in Figure 1. In Table 2, the “Distance” column is the position of the associated surface along the optical path from the first surface of the entrance window. The collimator and F/5 camera were designed to yield < 0.2 waves rms wave-front error across the full field and wavelength ranges. This was possible except in the *J* band, where in the field corners the error reaches 0.4 waves. A *J*-band corrector was designed and fielded, but found to be unnecessary in actual telescope use as the delivered point-spread functions (PSFs) with and without the corrector were indistinguishable. One unusual aspect of the design concerns the three thick lenses in the F/5 camera. Usually, glass thicknesses can be changed and compensated with air space changes, but here the elements’ thicknesses are important.

The F/17 camera has a longer optical path that was folded to fit into the same space as the F/5 camera, as shown in Fig. 1. Since the F/17 images nearly paraxial rays from the collimator, this camera is diffraction-limited. The pupil viewer allows the properties of the Lyot stop to be measured and optimized. Pupil viewer images and the Lyot stop are shown in Figure 2.

### 3.1. Lens Mounts and Baffles

Tolerance analyses of the optical designs yielded tight error budgets for lens positioning ranging from 12 to 100  $\mu\text{m}$ . In addition, during cooling and warming, CTE differences of the lenses and mounts create significant relative motions. Figure 3 shows one of the lens cells developed to address these issues. The lenses have ground flats on their outer diameters that are set against twin radial feet to achieve centration. These feet have dual radius toroidal surfaces: one radius matched to the lens outer diameter, the other small to ensure nearly perfect line contact with the lens. Located 120° from the feet, a flat steel spring holds the lens against the feet for all orientations. The spring allows relative motion of the lens and cell during thermal changes; the feet supply reference surfaces for the lens at operating temperatures.

To locate the lens along the optical axis, the inside front of the cell provides a circle of line contact for the lens front surface (see Yoder 1995). The rear lens surface is normally also ground in fabrication, and a wave washer steel spring is held against this surface by a snap ring. The wave washer takes up CTE length changes while keeping the lens in contact with the front reference surface. Stiction between lens crystals and cells would lead to unacceptable stresses during cooling and warming. Hence, all critical dimension interfaces have a 1 mil (25  $\mu\text{m}$ ) thick Kapton (polyvinylamide) layer and all noncritical interfaces (e.g., steel springs) contain 5 mil (125  $\mu\text{m}$ ) thick Kapton tape. The pattern

<sup>2</sup> See the Boston University Web site: <http://physics.bu.edu/SIF/>.

TABLE 1  
REQUIREMENTS SUMMARY

| Requirement Name                | Requirement Value                            | Achieved Value                             | Comment  |
|---------------------------------|--|--|--|
| Astronomical                    |  |  |  |
| Instrument capabilities .....   | Imaging mode                                 | ✓  |  |
|                                 | Spectroscopy mode                            | ✓  |  |
|                                 | Polarimetry mode                             | ✓  |  |
|                                 | Two plate scales                             | F/5 and F/17                               | Large-area surveying (wide), <i>L</i> and <i>M</i> imaging (narrow)        |
|                                 | Rapid mode changes (< 10 s)                  | 2–5 s                                      | High efficiency, good calibration, spectrophotometry                       |
| Field of view (wide) .....      | > 5'   | 10' × 10'                                  | Efficient Galactic plane mapping   |
| Pixel scale (wide) .....        | < 0.6" pixel <sup>-1</sup>                   | 0.59" pixel <sup>-1</sup>                  | Optimal sampling of median seeing  |
| Pixel scale (narrow) .....      | < 0.2" pixel <sup>-1</sup>                   | 0.18" pixel <sup>-1</sup>                  | <i>L</i> and <i>M</i> imaging, oversampling <i>K</i> -band diffraction PSF |
| Wavelength range .....          | 1–5 μm                                       | ✓  | Meet science requirements  |
| Detector array .....            | Sensor—InSb                                  | ✓  | Meet wavelength range  |
|                                 | Format—1024 × 1024                           | ✓  | Meet pixel, field-of-view requirements                                     |
| Broadband filters .....         | <i>J, H, K<sub>s</sub>, L', M'</i>           | ✓  | Galactic science, star formation   |
| Narrowband filters .....        | ...  | H <sub>2</sub> 2.122 μm on, off            | Star-forming regions   |
| Spectral resolutions .....      | Moderate ( <i>R</i> ~ 500–700)               | ✓ ( <i>JHK, LM</i> grisms)                 | Pluto ice features, stellar spectral typing, emission lines                |
|                                 | Low ( <i>R</i> ~ 50–100)                     | ✓ (SED grism)                              | Asteroids, SEDs  |
| Free spectral ranges .....      | One octave across <i>JHK</i> band            | 1.17–2.32 μm                               | Pluto ice, spectral typing   |
|                                 | One octave across <i>LM</i> band             | 2.8–5.5 μm                                 | Solid state features, emission lines                                       |
| Slit height (wide) .....        | > 30"  | 5'   | Solar system bodies, star formation regions, galaxies                      |
| Slit height (narrow) .....      | ...  | 3'   |  |
| Slit widths (wide) .....        | Matched to seeing                            | 1.2", 1.8", 2.4", 3.6"                     | Spans good to poor seeing  |
| Slit widths (narrow) .....      | Matched to diffraction                       | 0.36, 0.54, 0.72, 0.90, 1.08               | 2–6 pixels at F/17   |
| Polarimetric analysis .....     | Rotating HWP + Fixed Wire Grid               | ✓ ( <i>H</i> -band HWP) + 1–5 μm Wire Grid | Magnetic field mapping   |
| Instrumental polarization ..... | < 0.5%                                       | 0.35% ave                                  | Moderate precision polarimetry   |
|                                 | No optical folds before wire grid            | Single axis refractive design              |  |
| Optical and Physical            |  |  |  |
| Input F/No. ....                | 17.5   | ✓  | Existing Perkins Telescope Optics  |
| Optical design .....            | Reimaging, refractive                        | ✓  | To meet length limit, polarization requirements                            |
| Image quality (wide) .....      | Wave front error < 0.2 waves                 | all, except <i>J</i> band (0.4 waves)      | Instrument not to degrade delivered seeing                                 |
| Image quality (narrow) .....    | Strehl > 0.8                                 | all, except <i>J</i> band (0.6)            | Permit diffraction-limited imaging   |
| Spectroscopic design .....      | Single grism dispersion                      | ✓  | Largest free spectral range + moderate resolution                          |
|                                 | +order selection filters                     | 1.17, 1.85, 2.8 μm long-pass filters       | Reduce order overlap, select interest region                               |
| Pupil diameter .....            | 25 mm  | ✓  | Allow for 4 filter wheels with 50 mm diameter filters                      |
| Pupil aberration .....          | Achromatic                                   | ✓  | Single Lyot stop across 1–5 μm range                                       |
| Ghosting .....                  | In-focus ghosts < read noise                 | ✓  | No spurious stellar images   |
|                                 | No out of focus ghosts for unsaturated stars | ✓  | Backgrounds astronomical, not instrumental                                 |
| Length .....                    | < 1 m  | ✓  | Avoid floor, pier collisions   |
| Weight .....                    | < 360 kg                                     | ✓  | Stiffness Limit of Mount   |
| Operational                     |  |  |  |
| Usage pattern .....             | Facility-class                               | Routine scheduling; always available       | Multiple users, including visitors   |
| Alignment .....                 | Optics—By design                             | ✓  | No adjustments   |
|                                 | Instrument—Bolt and go                       | ✓  | Easy, noncritical telescope mounting                                       |
| Cooling .....                   | Durations: > months                          | ✓ (Closed-cycle CTI 1050)                  | No cryogenics, stable optics, detector                                     |
|                                 | Optics: < 75 K                               | 65–73 K                                    | No instrumental background to 5.5 μm limit of detector                     |
|                                 | Detector: < 38 K                             | 33.5 K                                     | Low dark current for InSb sensor   |

NOTE.—Check denotes requirement met.

of the interface Kapton consists of a long rectangular strip to wrap around the outer diameter of the lens, with “fingers” of Kapton extending forward (Fig. 3a).

The assembled lens cells were located via precision bores, reference shelves in the bores, and precision flats on the lens cells. Three small ball bearings located around each lens cell

located it inside a bore hole. Cells and spacers were stacked against a reference shelf in a bore and the stack held in place by a final wave washer and snap ring.

Figure 4 shows the structures inside the Mimir cryostat. Aggressive baffling controls stray light and ingress of unwanted thermal radiation. Interlocking pieces form light-tight optics

units; tight clearances separate moving mechanisms; and numerous individual and multiple layer baffles are within the optical system.

The detector unit is mounted to the 70 K filter box through four G10-type fiberglass-epoxy “V” tabs. This unit is surrounded by a cover mounted in a groove in the back of the filter box. The detector is mounted in a Mauna Kea Infrared Labs (Honolulu, HI; MKIR) designed and fabricated aluminum block, containing the array socket mount, fanout printed circuit cards, interface connectors, and an array mask baffle.

### 3.2. Light Analysis

The light analysis components of Mimir consist of the slit-decker unit, the four filter wheels, and the detector array. In Figure 4, the first (POL) and second (FW1) wheels bracket a bulkhead in the filter box. The FW2 and FW3 wheels bracket another bulkhead, which contains the Lyot stop at the pupil. Filters, half-wave plates, and the wire grid are mounted in their cells using Kapton interfaces, wave springs, and snap rings. Grism cells include three hard steel pins providing reference surfaces and subcells allowing rotational alignment. The initial filter complement in Mimir is summarized in Table 3. The broadband  $JHK_sL'M'$  filters are from the Mauna Kea Observatories (MKO) NIR set (Simons & Tokunaga 2002; Tokunaga et al. 2002; Tokunaga & Vacca 2005). FW1–3 each hold up to nine filters in cells plus an open. The four filter wheels are coaxial, with a nested axis hub and forward located drive gears (see Fig. 5).

The POL wheel holds up to five rotating half-wave plates in cells plus an open. Each cell is located by an annular trough engaging three cylindrical ball bearing races, two of which are hard-mounted and one of which is held by a flex-pivot arm (see Fig. 5a). When the wheel is rotated to position a POL cell into the optical beam, a gear atop the freely rotating cell engages a motor-driven gear, located under the optical axis. The motor rotates the selected POL cell, enabling half-wave plate positioning. The zero-order half-wave plate for  $H$  band consists of two orthogonally-oriented  $MgF_2$  flats manufactured by NovaPhase (Newton, New Jersey) and assembled into a custom HWP cell.

Polarimetry involves multiple cycles of image collection and half-wave plate positioning. Using this method, Stokes  $U$  and  $Q$  images are constructed from pairs of images obtained through specific half-wave plate rotation angles. The cold, rotating HWP plus cold wire grid analyzer permit full  $10' \times 10'$  wide-field imaging linear polarimetry, a capability not met or surpassed by any other infrared instrument. Since the wire grid functions across the entire 1–5  $\mu m$  wavelength range, implementing polarimetry outside  $H$  band only requires insertion of other zero-order or achromatic half-wave plates.

For spectroscopy, a slit and the decker opening are positioned on the optical axis and an appropriate long-pass filter is selected via the filter wheels. The slit-decker unit (see Fig. 6) consists of two plates on movable cars. In imaging mode, both

TABLE 2  
OPTICAL PRESCRIPTIONS

| Designation         | Material         | Radius (mm) | Thickness (mm) | Distance (mm) |
|---------------------|------------------|-------------|----------------|---------------|
| Window .....        | ZnSe             | Flat        | 25.0000        | 0.0000        |
|                     |                  | Flat        | 85.0000        | 25.0000       |
| Focus .....         |                  | ...         | 24.9978        | 110.0000      |
| Collimator          |                  |             |                |               |
| Col L1 .....        | ZnS              | 134.0013    | 12.3181        | 134.9978      |
|                     |                  | 109.0043    | 8.4767         | 147.3159      |
| Col L2 .....        | BaF <sub>2</sub> | 114.1446    | 30.8086        | 155.7926      |
|                     |                  | −415.9523   | 83.8997        | 186.6012      |
| Col L3 .....        | LiF              | −157.4518   | 30.3362        | 270.5009      |
|                     |                  | −2193.8782  | 173.7924       | 300.8371      |
| Col L4 .....        | ZnSe             | −58.0310    | 16.9595        | 474.6295      |
|                     |                  | −70.8165    | 2.3305         | 491.5890      |
| Col L5 .....        | BaF <sub>2</sub> | 1985.0647   | 11.6218        | 493.9195      |
|                     |                  | −135.2759   | 2.4785         | 505.5413      |
| Col L6 .....        | LiF              | 49.9567     | 9.8799         | 508.0198      |
|                     |                  | 41.6469     | 112.0800       | 517.8997      |
| Pupil .....         |                  |             |                | 629.9797      |
| F/5 Camera          |                  |             |                |               |
| F/5 L1 .....        | BaF <sub>2</sub> | 138.0744    | 11.2928        | 709.4605      |
|                     |                  | −74.1262    | 1.9977         | 720.7533      |
| F/5 L2 .....        | ZnSe             | −3374.3284  | 33.3897        | 722.7510      |
|                     |                  | 955.6229    | 15.6458        | 756.1407      |
| F/5 L3 .....        | LiF              | −43.0219    | 7.5915         | 771.7865      |
|                     |                  | −78.7508    | 2.0554         | 779.3780      |
| F/5 L4 .....        | ZnS              | 160.4485    | 31.8291        | 781.4334      |
|                     |                  | 178.6468    | 2.0000         | 813.2625      |
| F/5 L5 .....        | BaF <sub>2</sub> | 61.2129     | 37.3371        | 815.2625      |
|                     |                  | 46.3973     | 37.3778        | 852.5996      |
| Detector .....      | InSb             |             |                | 889.9774      |
| F/17 Camera         |                  |             |                |               |
| F/17 L1 .....       | BaF <sub>2</sub> | 837.3945    | 6.3790         | 760.1239      |
|                     |                  | −81.4320    | 8.4086         | 766.5029      |
| F/17 L2 .....       | LiF              | 38.8759     | 7.0314         | 774.9115      |
|                     |                  | 29.1512     | 8.0602         | 781.9429      |
| F/17 L3 .....       | ZnSe             | 108.3772    | 6.0028         | 790.0031      |
|                     |                  | 70.9983     | 46.9228        | 796.0059      |
| F/17 L4 .....       | ZnS              | 57.8339     | 8.5517         | 842.9287      |
|                     |                  | 65.7413     | 348.4992       | 851.4804      |
| Detector .....      | InSb             | ...         | ...            | 1199.9796     |
| Pupil Viewer Camera |                  |             |                |               |
| PV L1 .....         | ZnSe             | 178.0263    | 3.5170         | 778.6375      |
|                     |                  | −266.3401   | 72.5565        | 782.1545      |
| PV L2 .....         | ZnSe             | 47.1394     | 3.487          | 854.7110      |
|                     |                  | 96.9653     | 31.7854        | 889.9834      |

slit and decker cars are driven out of the optical path. The slit car holds a thin beryllium-copper sheet mask, photoetched to contain 5' “tall” and 3' “short” slits, with a range of slit widths, and

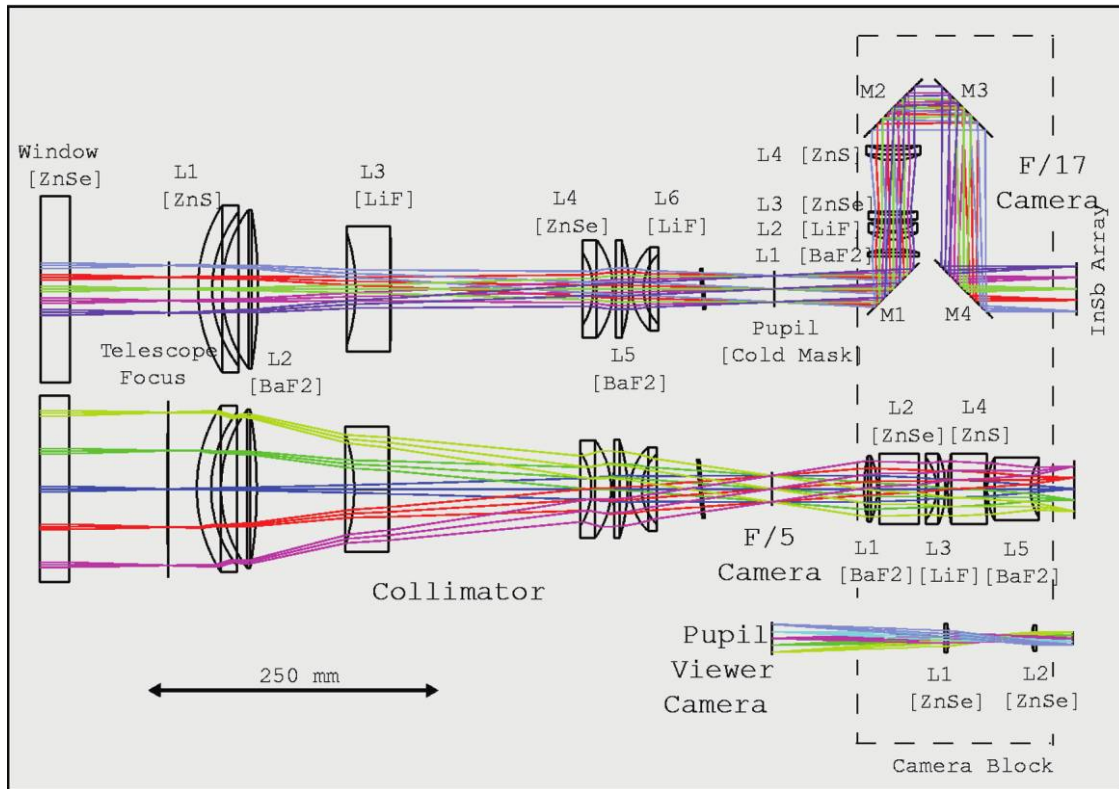


FIG. 1.—Mimir optics summary ray tracing. Upper configuration shows light path through cryostat window, six-lens collimator, and four-lens plus four-mirror F/17 camera. Middle configuration shows F/5 wide-field option with five-lens camera. Bottom trace shows two-lens pupil camera. Dashed rectangle indicates that the F/17, F/5, and pupil viewer optics are contained in the camera block unit; selection is by motion of the block perpendicular to the optical axis. Scale bar is at lower left. Total length from front of cryostat window to detector is about 0.9 m.

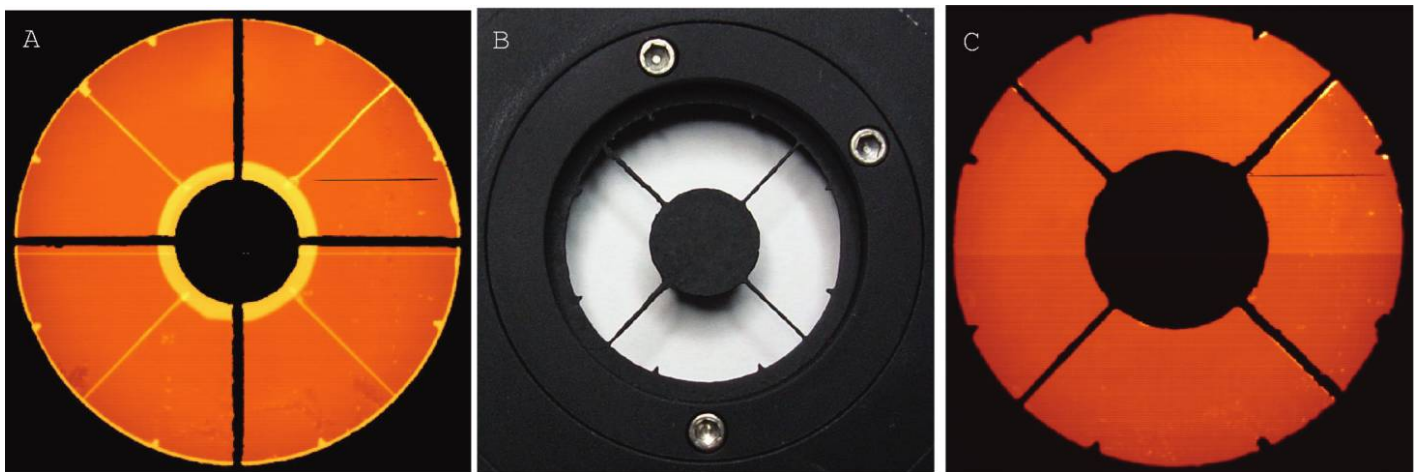


FIG. 2.—Pupil images and pupil mask. (a) Pupil image obtained during first light observations. Color scale reveals high emissivity surfaces as yellow-white, cold masked surfaces as black, and intermediate emissivity as orange. Note spider locations, large diameter secondary, and outer diameter features in this minimally masked image. (b) Photograph of the cold mask fabricated based on the first light image, mounted in pupil mask holder. (c) Pupil image obtained using the new mask. Nearly all the features in (a) have been masked in the new image. The horizontal linear black streak in the upper right is a detector artifact. The 16 spikes around the outer diameter are due to mirror cover petal fixtures.

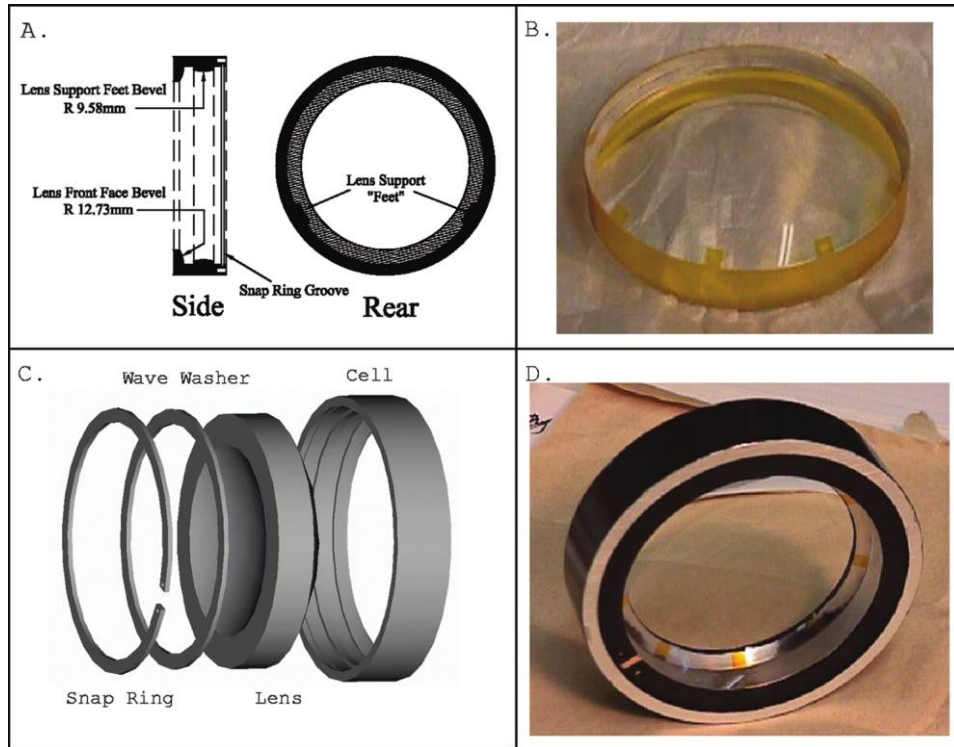


FIG. 3.—Lens cell details. (a) Two 2D views of basic lens cell, showing two radial support “feet” and front and side mount surfaces as torii of revolution. (b) F/5 camera first lens (BaF<sub>2</sub>) with yellow Kapton spacer wrapped around outer diameter with rectangular “fingers” extending over the front edge of the lens. (c) Oblique rendering of lens cell, lens, and wave washer snap-ring. Kapton spacers are not shown. (d) Assembled F/5 lens cell, viewed from back. Note the Kapton fingers between the front lens surface and the lens cell front reference surface. The front and back surfaces of the lens cell are ground and lapped for precision location against either a reference surface in the bore or neighboring lens cells or spacers.

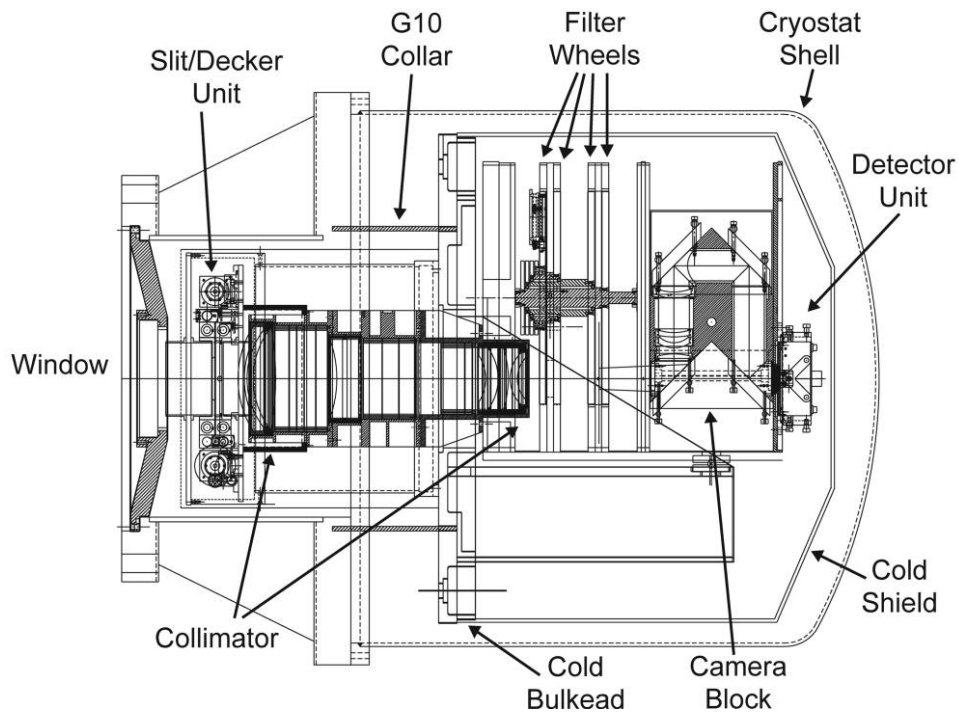


FIG. 4.—Mimir AUTOCAD side view drawing of full instrument, with major components identified.

TABLE 3  
MIMIR FILTER WHEEL COMPLEMENT

| Designation | Position | Name                 | Description  |
|-------------|----------|----------------------|--|
| POL .....   | 1        | Dark                 |  |
|             | 2        | F/5 Baffle           | Square opening with rounded corners                                  |
|             | 3        | Open                 |  |
|             | 4        | <i>H</i> -HWP        | <i>H</i> -band zero-order half-wave plate                            |
|             | 5        | Open                 |  |
|             | 6        | F/17 Baffle          | Round opening  |
| FW1 .....   | 1        | Dark                 |  |
|             | 2        | <i>J</i>             | MKO-IR <i>J</i> -band  |
|             | 3        | <i>H</i>             | MKO-IR <i>H</i> -band  |
|             | 4        | <i>K<sub>s</sub></i> | MKO-IR <i>K<sub>s</sub></i> -band                                    |
|             | 5        | <i>L'</i>            | MKO-IR <i>L'</i> -band   |
|             | 6        | <i>M'</i>            | MKO-IR <i>M'</i> -band   |
|             | 7        | PK-50                | Blocker longward of 2.8 $\mu\text{m}$                                |
|             | 8        | H <sub>2</sub> -on   | 1% wide, 2.1198 $\mu\text{m}$ H <sub>2</sub> S(1) line center filter |
|             | 9        | H <sub>2</sub> -off  | 1% wide, 2.0896 $\mu\text{m}$ center comparison filter               |
|             | 10       | Open                 |  |
| FW2 .....   | 1        | Dark                 |  |
|             | 2        | Open                 |  |
|             | 3        | 1.17 LP              | 1.17 $\mu\text{m}$ cut-on long-pass filter                           |
|             | 4        | 1.85 LP              | 1.85 $\mu\text{m}$ cut-on long-pass filter                           |
|             | 5        | Open                 |  |
|             | 6        | PK-50                | Blocker longward of 2.8 $\mu\text{m}$                                |
|             | 7        | Open                 |  |
|             | 8        | 2.8 LP               | 2.8 $\mu\text{m}$ cut-on long-pass filter                            |
|             | 9        | Open                 |  |
|             | 10       | <i>K<sub>s</sub></i> | MKO-IR <i>K<sub>s</sub></i> band, second copy                        |
| FW3 .....   | 1        | Dark                 |  |
|             | 2        | <i>JHK</i> Grism     | 120 lines $\text{mm}^{-1}$   |
|             | 3        | Open                 |  |
|             | 4        | SED Grism            | 14.3 lines $\text{mm}^{-1}$  |
|             | 5        | Open                 |  |
|             | 6        | Open                 |  |
|             | 7        | Open                 |  |
|             | 8        | <i>LM</i> Grism      | 50 lines $\text{mm}^{-1}$  |
|             | 9        | Wire-Grid            | IGP227 (Molelectron Detector: Portland, OR)                          |
|             | 10       | Open                 |  |

treated with nickel-based chrome blackening. The decker car contains a single tall, knife-edged, 25" by 5.3' opening. When it is over the optical axis, only one slit scene is illuminated. Moving both the decker and slit cars onto the optical axis takes a few tens of seconds, with motions to neighboring slit scenes requiring only 1 or 2 s.

The detector is an ALADDIN III InSb photovoltaic layer bump-bonded to a silicon CRC206 readout device, manufactured by Raytheon. Details regarding our device (416173) are found in Table 4.

#### 4. MECHANICAL, CRYOGENIC SYSTEMS

The Mimir optical system assembles into a single, mechanically rigid, and light-tight unit consisting of the collimator and the filter-camera box. The filter-camera box was fabricated as individual flat plates and dip brazed (see Fig. 7). The combined collimator + filter-camera box optical system is located via a five-point kinematic mount. The optical system is referenced through the kinematic mounts to the internal cold bulkhead. This bulkhead is referenced to the warm bulkhead and telescope mounting flange through the G10 fiberglass-epoxy

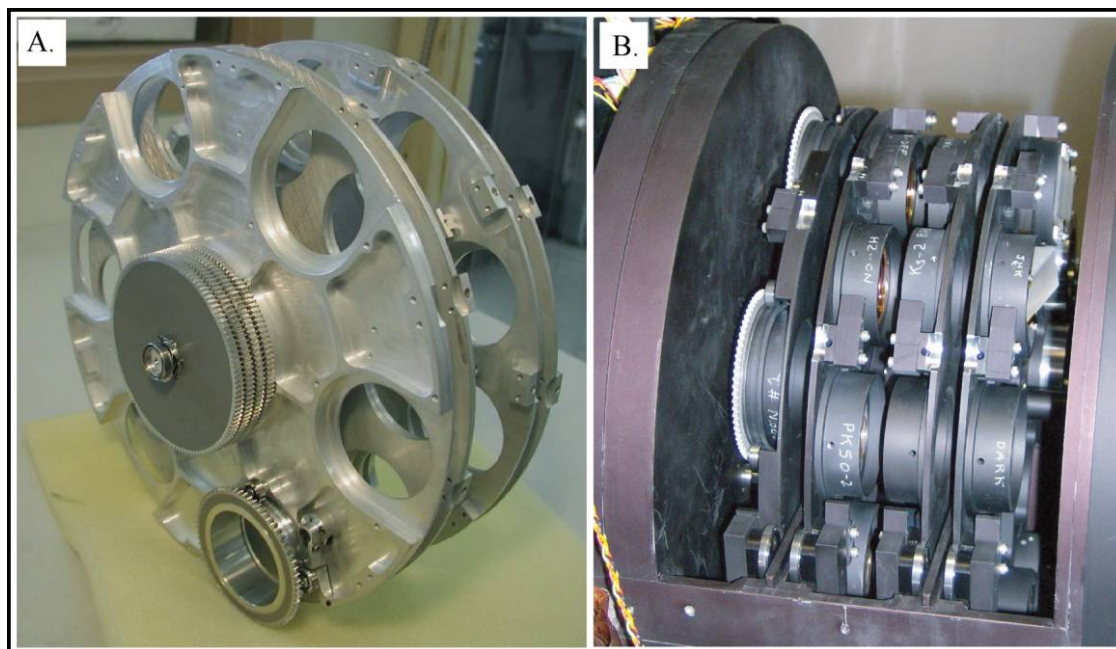


FIG. 5.—Nested filter wheels in Mimir. (a) Assembled filter wheel system, including one empty POL wheel HWP cell, before bead blasting and anodizing. (b) Populated filter wheels, as mounted in Mimir. POL wheel is at left, FW3 at right. Note wedged *JHK* grism in FW3.

collar, itself epoxied into grooves in the cold and warm bulkheads (see Fig. 4).

The cryogenic components consist of passive and active cold shields and the closed-loop helium refrigerator system. Forward and rearward of the cold bulkhead, two active cold shields (65–75 K) surround the optical system, forming light-tight covers. These are surrounded by passive shields consisting of thin G10

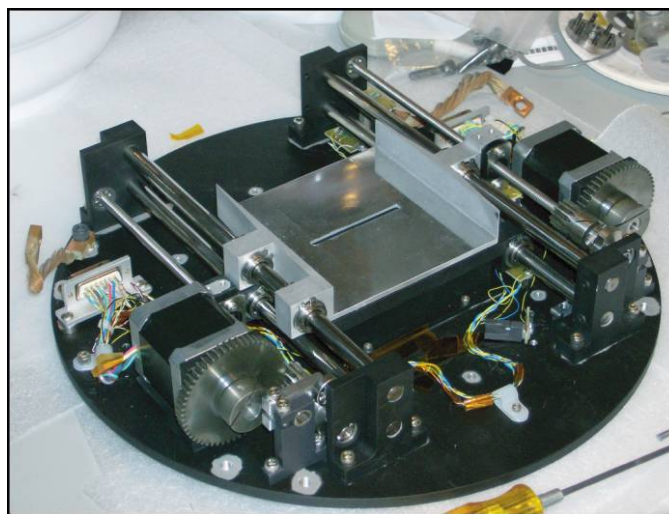


FIG. 6.—Slit-decker unit. The decker car is highly polished aluminum; the slit car is partially hidden under the decker car.

cylindrical forms wrapped with 120 layers of aluminized mylar (MLI). The remaining space where heat ingress could be a problem is the back of the warm bulkhead facing the cold bulkhead, where three passive stainless steel shields are positioned to intercept the radiation.

During operation, Mimir’s optics system is kept between 65 and 75 K by the first (50 K) stage of a CTI 1050 closed-cycle helium refrigerator head. Mimir’s detector is cooled to 28–40 K through connection to the second (10 K) stage of the cold head. The cryostat insulation system was tested prior to insertion of the cold head. The total heat load was 20 W, of which 9 W arrived via the G10 collar. The cold head is mounted to the warm bulkhead on a vibration isolator. Its first stage is attached to the cold bulkhead via copper straps. The second stage hosts a charcoal getter and 3.2 mm diameter copper rods connecting to the detector unit through a sapphire-disk and copper split-block electrical isolator. The detector cooling system was tuned to locate the desired 33.5 K operating point at about 30%–40% of the full power range of the control unit.

#### 4.1. Moving Mechanisms

Mimir has eight moving mechanisms, all within the cold vacuum volume. The mechanisms consist of either rotary (wheel) or linear motions. They all use low-cost stepper motors that have been cleaned of lubricants and tested under vacuum cryogenic conditions.

TABLE 4  
SUMMARY OF MIMIR DETECTOR PERFORMANCE

| Quantity              | Value                 | Units                                 | Description                    |
|-----------------------|-----------------------|---------------------------------------|--------------------------------|
| Detector              | ALADDIN III           |                                       | InSb + CRC206 Si readout       |
| Format                | 1024 × 1024           | pixels                                |                                |
| Pitch                 | 27                    | μm                                    | Square                         |
| Operating temperature | 33.5                  | K                                     |                                |
| Conversion gain       | 8.21                  | e <sup>-</sup> ADU <sup>-1</sup>      |                                |
| Well depth            | ~60–180,000           | e <sup>-</sup>                        | “Sweet spot” - “deep wells”    |
| Read noise            | 18–20                 | e <sup>-</sup> rms                    | Single read; CDS 1.4× higher   |
| Q.E.                  | 90 ± 3                | %                                     | Raytheon Lab value             |
| Dark current          | 0.98 ± 0.27           | e pixel <sup>-1</sup> s <sup>-1</sup> | Raytheon Lab value             |
|                       | 22.65 t <sup>-1</sup> | e pixel <sup>-1</sup> s <sup>-1</sup> | Mimir measured (t = 0.3–120 s) |
| Operability           | 99.8                  | %                                     | 2500 dead pixels               |
| Reverse bias          | -0.85                 | V                                     | See text                       |
| Residual image        | <0.01                 | %                                     | Not measurable                 |
| Global reset duration | 2.56                  | μs                                    |                                |
| Reset—read offset     | 20                    | μs                                    | Optimal for no residual image  |

The filter wheels and half-wave plate rotator have stepper motors and gear reduction sets, with flex-pivot based detents on the outer diameter of each filter wheel. Samarium-cobalt magnets in each detent arm are sensed by reed switches to provide detent knowledge. Each filter position is four-bit encoded using magnets and reed switches. Half-wave plate zero angle sensing uses a magnet in each HWP cell and a reed switch in the bulkhead. Drive times between neighboring filter wheel positions is under 1 s.

The linear motion units, the slit-decker cars, and the camera block are configured to sense motion range limits. These units use stepper motors to drive lead screws attached to the slit-decker cars or the camera block. The slit-decker drive systems produce a linear motion of 5 μm (0.03" on the sky) per motor step. The lead screw has a detent system (see Fig. 6) with a

magnet-reed switch sensor and operates at 67 motor steps per detent position. Slit scenes are offset from each other by 20 detent positions (43").

The camera block drive unit has a magnet-reed switch sensor to report each lead screw rotation. This drive gives 3.6 μm of motion across the optical axis per motor step, but no detent action. An electromechanical brake holds the camera in place when not powered, providing enough torque to prevent the 9 kg camera block from counterdriving the lead screw.

## 5. ELECTRICAL & CONTROL

### 5.1. Detector Array Control

Mimir represents the first implementation of the Astronomical Research Cameras (ARC; San Diego, California)

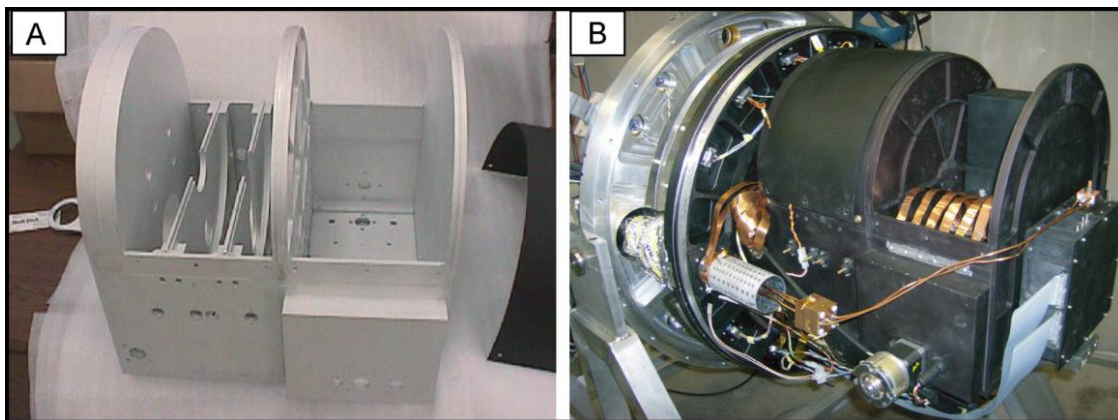


FIG. 7.—Mimir’s filter-camera box unit. (a) After dip-brazing, the filter-camera box was a single, stiff, lightweight unit. (b) The post-brazed unit was black anodized and populated with filter wheels and camera block and is shown mounted behind the cold bulkhead. The second stage getter, thermal transport copper rods and split copper block, and the ribbon cables to the detector unit are all visible. The camera block drive motor and electromagnetic brake are on the lower side of the camera bay. The camera bay cover is off to show the thermal strapping to the camera block.

Generation III array controller system with an ALADDIN III detector array. The 32 output signal lines from the detector array are carried by manganin ribbon cables to the warm bulkhead, then along warm coaxial lines to the array controller, through an internal fanout board, and onto four 8-channel fast analog to digital (A/D) boards (16 bits;  $2 \mu\text{s}$  A/D conversion time). A goal was to run the ALADDIN III array at nearly its maximum frame rate (15 Hz) under high background conditions. The 250 MHz fiber communication between the serial board in the ARC controller and the PCI-based board in the control computer limits Mimir's full frame rate to 12.5 Hz. The actual time needed for signal levels to stabilize and prevent pixel cross-talk is about  $5 \mu\text{s}$ : Mimir is operated at  $7.5 \mu\text{s}$  per pixel read time. Faster frame rates are achieved for subarray readouts.

## 5.2. Motion, Thermal and Vacuum

Temperatures in Mimir are monitored continuously and reported to a conveniently accessed Web site. These include the ambient air and cryostat window, cold head first and second stages, cold bench, filter-camera box, and camera block. All are obtained from silicon diodes and a Lake Shore LS218 monitor unit. The detector temperature is controlled using a Lake Shore LS331 unit. For cold head second stage temperatures of 17–25 K, with about 0.2 K of thermal noise, the detector array experiences temperature stability values of 1–3 mK rms at 33.5 K. The vacuum in the main cryostat is continuously monitored using a thermocouple vacuum gauge and a Bayer-Alpert high vacuum gauge. Mimir operates with a typical vacuum of  $(0.4\text{--}2) \times 10^{-9}$  torr.

Motor unit motion, encoding, limit, and brake control is provided by eight identical control units, each connected to one motion-sensing unit. Each control unit has a Pontech STP100 stepper motor controller board attached to a custom printed circuit board that provides limit condition, brake signal processing, and 5 sensing bits. All motion control units are connected via a daisy chain RS422 protocol and there to a single RS232 signal line. The RS232 signal lines from the motion control units, the temperature units, and the vacuum control unit are sent via an 8-channel multiplexer along a fiber pair to the warm control room, demultiplexed, and input to a second, control computer. The two Mimir computers reside on the common ethernet line at the Perkins telescope. Mimir operation is controlled and coordinated by LOIS (Lowell Observatory Instrument Software; Taylor et al. 2000, 2004).

## 6. OPERATING MODES

Mimir operates in three main modes: imaging, spectroscopy, and polarimetry. A fourth, minor, mode is use of the pupil viewer camera. Within each main mode there are two camera and plate scale options: the F/5 camera with  $0.59'' \text{ pixel}^{-1}$  image sampling and the F/17 camera with  $0.18'' \text{ pixel}^{-1}$  sam-

pling. For spectroscopy, there are 13 slit choices as well as slitless operation.

The ALADDIN III array detector is also operated in multiple modes, distinguished by reverse bias voltage setting, image size, and readout mode. The reverse bias settings will produce either clean cosmetics with low dark current or deep electron well depths in the pixels. Images are read out as a full array or as a rectangular central subarray, down to sizes as small as  $32 \times 32$  pixels. Subarrays are useful for improving the array read and reset cadence, as required for high-background  $L'$  and  $M'$  imaging, occultation studies, and bright object spectroscopy.

Normal, low-background readout of the array consists of application of a short global reset signal, a short dwell to permit charges to finish sloshing, a first nondestructive read of all pixels, integration, and a second nondestructive read. Differencing the pixel values of the two reads results in a correlated-double-sampled (CDS) image. Alternatively, multiple reads ("Fowler sampling") may be used. For very bright backgrounds, the first CDS read may be eliminated to produce a reset-integrate-read cycle.

## 7. PERFORMANCE

### 7.1. Detector Array

Operating conditions and detector array performance for Mimir's detector are summarized in Table 4. Mimir has a conversion gain of  $8.21 e^- \text{ ADU}^{-1}$ ,  $18 e^-$  rms single read noise, and a well depth of about 60,000  $e^-$  for the "sweet spot" reverse bias setting (see below).

A sweep of detector temperature (Fig. 8) revealed that operation at about 33.5 K was optimal as a good compromise between

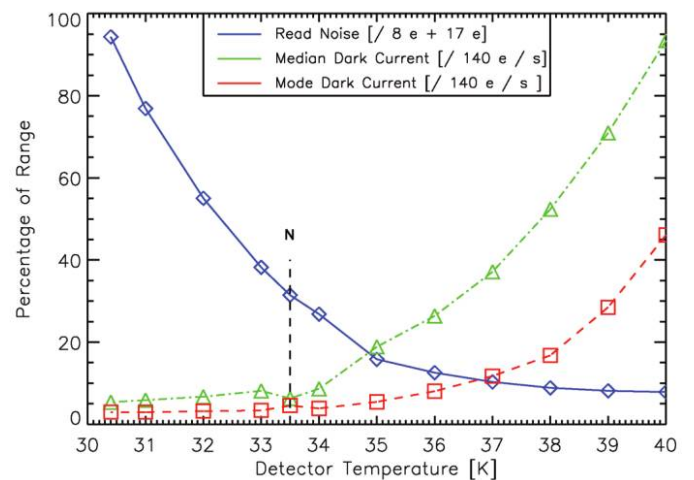


FIG. 8.—Comparison of measured single readout rms noise and dark current vs. detector temperature. At lower temperatures, read noise increases, and at higher temperatures, dark current increases. Mimir is normally operated at 33.5 K (vertical dashed black line labeled “N”), just below the onset of higher dark current.

rising read noise at lower temperatures and rising dark current at higher temperatures. The dark current seen in Figure 8 is higher than measured by Raytheon and is not linear with time, but decays as the inverse of the integration time (see Table 4). For long integration times, the *differential* dark current is very low, approaching the value measured by Raytheon. Shown in Figure 8, however, are the total dark counts measured in 100 s, divided by that time, which overestimates the asymptotic dark current.

A detector reverse bias voltage sweep was used to pick two useful operating points. In Figure 9, the full well depth increases with reverse bias level to about  $-1.5$  V, where breakdown begins. The median dark current also grows with reverse bias until about  $-1.5$  V, where it rises dramatically. Read noise shows no dependence on reverse bias and so is not plotted. A more important concern for image quality is the number of “hot” pixels. This was quantified by integrating the pixel value histogram beyond 3 times the rms value above the mean (*red, dashed curve*). A “sweet spot” associated with an unusually low hot pixel fraction, and so a very narrow dark current histogram, was found for a reverse bias in the range  $-0.8$  to  $-0.9$  V. This operating point corresponds to only about one-half of the maximum electron well depth of the ALADDIN III. To achieve deeper wells, a second bias point was selected at  $-1.35$  V, yielding around 180,000  $e^-$  wells. The dark current is higher than for the sweet spot, but for short exposures it will not limit observations.

Residual images are not a problem for Mimir. Tuning the global reset duration and dwell time before the first readout eliminated residual images to below measurable levels. We infer that residual image problems seen in other ALADDIN III and II implementations (e.g., SpeX; Rayner et al. 2003) are due to charge sloshing of the reset electrons, coupled with inadequate dwell time for the sloshing to cease.

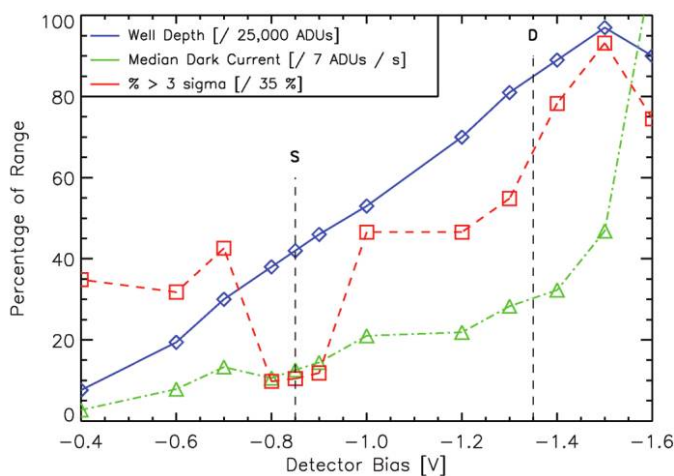


FIG. 9.—Comparison of measured pixel well depth, dark current, and hot pixel count vs. detector reverse bias, as generated at the array controller. Two useful operating points are identified, corresponding to the conditions producing the lowest hot pixel count (the “sweet spot”; vertical dashed black line labeled “S”) and the deepest wells (vertical dashed line labeled “D”).

The fixed pattern of bad pixels in our array totals about 2500 pixels, representing only about 0.2% of the total pixels. About half of this was caused by a rapid cooling event that introduced a spectacular crack spanning all four quadrants of the array. As operability of the remainder of the pixels is unaffected after several cooling and warming cycles, we deduce that the crack is in the InSb photovoltaic material and not in the silicon readout or the ceramic substrate.

## 7.2. Detector Operation: Linearity Correction Method

Meeting the goal of precision polarimetry of weakly polarized signals requires that the detector array yield signals accurate to within the expected photometric uncertainties to the limits of the well depths. InSb photoconductors have nonlinear responses to light that must be accurately corrected so as not to corrupt the weak polarization signals sought. The linearity correction method advocated by Vacca et al. (2003) is able to correct ALADDIN III array signals to about 1% uncertainty levels. Unfortunately, this level is similar to the average polarization *signal* level expected at *H* band—Mimir’s linearity correction must be significantly better.

One of the chief limitations of the Vacca et al. method is due to an inherent loss of critical information in their data collection process. Their array control electronics forms the CDS image difference of the two array readouts on the fly and does not save the individual readout images. The count level for each pixel is not referenced to the counts present just after release of the global reset signal. Depending on the scene or stellar illumination, many pixels could be already into the nonlinear portion of their response *before* the start of the integration period. Their method attempts to iteratively recover the missing information, but the end result is unsatisfactory for our polarimetric application.

Mimir’s ARC Gen III controller and LOIS software are able to save all readouts of the array, and we have used this full information to develop a robust linearity correction that provides full Poisson-limited correction to the full well depth. It relies on use of the two readouts in a CDS image plus the initial readout obtained for a dark image to reference all pixel counts to the reset release time of each image. It first corrects each of the two constituent images for nonlinearity and then computes the *true* CDS difference image. The correction calibration is based on characterizing the response of each pixel in the detector to a stepped series of illumination levels, obtained from imaging an in-dome illuminated flat-field screen. The following discussion is aided by reference to Figure 10.

The steps followed are

1. Select an internal dark filter in one filter wheel. Obtain first (D1) and second (D2) readouts. D1 will act as the best proxy for the image after the reset signal has been released (RR).<sup>3</sup>

<sup>3</sup> An image obtained *during* reset or immediately after release of the reset signal is not equivalent to the RR image, due to current and voltage transients

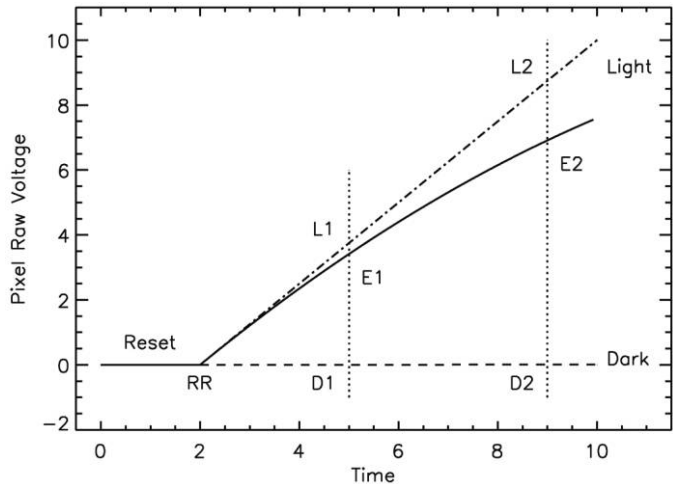


FIG. 10.—Model of time dependence of the photoconductor voltage for 1 pixel under dark and light conditions. The vertical dotted lines indicate the first and second readout times for this pixel. “RR” indicates the pixel value present at the release of the reset signal, “D1” is the value measured for the pixel during the first read for the no light condition. The parabolic curve passing through “E1” and “E2” simulates a normal nonlinear response of the InSb. The line through “L1” and “L2” represents the linearity-corrected version of the response. Note that by E1, this pixel is already significantly nonlinear, showing the importance of referencing the linearity correction back to the RR condition.

2. Select a nondark filter, and view an illuminated flat-field screen. Obtain a series of exposures, spanning the shortest exposure time possible to well past saturation of all image pixels. For Mimir, we normally use 25–50 different flat-field exposure times ( $t_{FF}$ ) to map the nonlinearity. Each image generates a first (E1) and second (E2) readout, the difference of which is the “classical” CDS image.

3. Compute difference images between each E1 readout of the illuminated images and the D1 reference image. This forms (E1-RR), a CDS-like image that carries information about the photons already detected by the array *before* the formal start of the integration period.

4. Add the (E1-RR) image to its corresponding (E2-E1) CDS image to form an (E2-RR) image. This references the image exposed at the E2 time back to the RR condition.

5. For each (E2-RR) pixel in the 25–50 flat-field exposure image set, examine the run of apparent counts versus exposure time to identify the onset of saturation. This is seen as a strong decrease in the count rate beyond some  $t_{FF}$ .

6. For the run of counts versus time up to within about 95% of saturation, fit the run with a polynomial. A fourth-order polynomial is needed to recover the true shape of the nonlinearity for Mimir, based on  $F$ -tests.

flowing in the device. All pixels begin integrating light upon release of the reset signal, so nonlinearity effects need to be referenced to RR, not to the first CDS science readout. The first science image readout occurs several charge-sloshing time periods after the RR condition and spans a full readout time of the array.

7. Invert the fit for each pixel to recover a *different* fourth-order polynomial of pixel value (in counts) that returns a nominal  $t_{FF}$  time.

8. Collect all of the saturation and fourth-order fit coefficients into nine linearity correction tables, as images. These are (1) the saturation value, in counts, for that pixel, beyond which no correction is possible; (2)–(6) the five coefficients of the first fourth-order polynomial of counts that yields a nominal  $t_{FF}$  value from the apparent count value; and, (7)–(9) the highest three coefficients of the second fourth-order polynomial that yields a count value from the nominal  $t_{FF}$  value. These last three coefficients represent the parabolic, cubic, and quartic corrections that when added to an image will correct the nonlinear behavior to yield a purely linear response.

Application of the correction to science data is as follows:

1. Dark images are taken near the same UT time as the science images

2. The science frame S1 images are differenced with the dark D1 images to produce (S1-RR) images.

3. For each pixel in the (S1-RR) image, compare against its saturation value. If exceeded, mark the pixel bad or deleted. If not exceeded, use fit coefficients (2) through (6) to compute the nominal  $t_{FF}$  value for the pixel. Note that this time is *unrelated* to the science image exposure time.

4. Use the  $t_{FF}$  value with coefficients (7) through (9) to compute the nonlinearity correction. Add this correction to the (S1-RR) pixel value to obtain (S1-RR)<sub>TRUE</sub>.

5. Repeat the process, computing the S2 science frame difference against the dark D1 image, checking saturation, computing the  $t_{FF}$  exposure times, computing nonlinearity corrections, and adding corrections to yield (S2-RR)<sub>TRUE</sub> difference images.

6. Compute the final, nonlinearity-corrected CDS image as the difference between the (S2-RR)<sub>TRUE</sub> and (S1-RR)<sub>TRUE</sub> images.

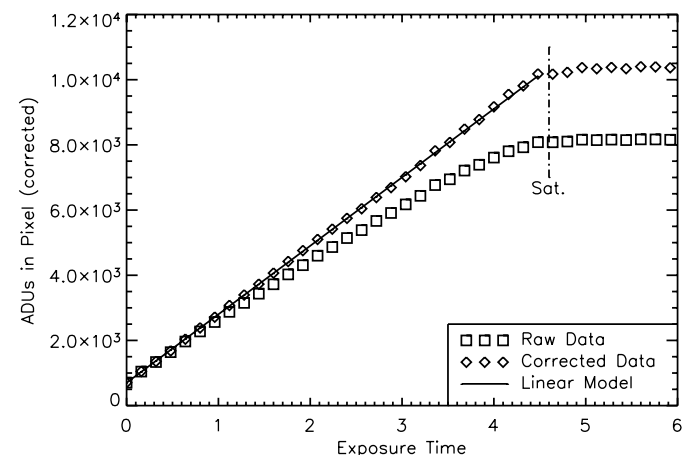


FIG. 11.—Run of uncorrected “classical” CDS (*squares*) and linearity-corrected true CDS counts (*diamonds*) vs.  $\tau_{FF}$  exposure time.

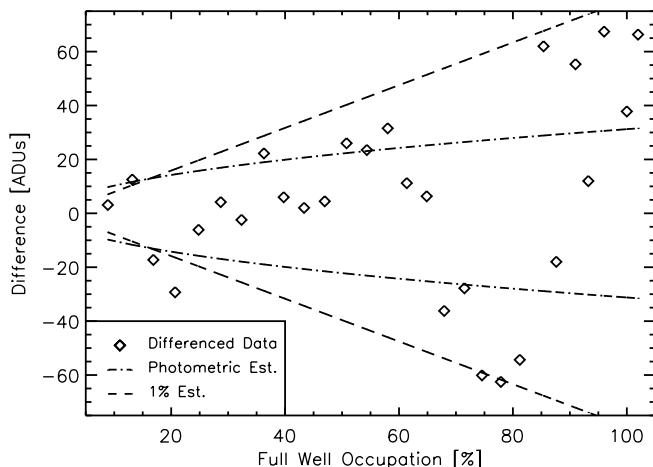


FIG. 12.—Comparison of corrected data deviations away from linear model vs. pixel counts, expressed as a percentage of the pixel full-well depth. Diamonds: Difference (residuals) of linearity-corrected data and predicted model linear behavior. Dot-dashed, inner lines: Envelope of expected rms differences, based only on photometric and read noise contributions. Dashed, outer lines: Envelope of differences, based on constant 1% error assumption. The linearity correction method outlined here returns data corrected to the limits of photometric uncertainty and better than the 1% quality standard.

Example corrected and uncorrected data values versus nominal  $t_{\text{FF}}$  times are shown for 1 pixel in Figure 11, where the linearity-corrected CDS values are represented by diamonds and the linear model fit to the collection of these corrected dome flat exposures is shown by the solid line.

The photometric quality of this correction method is shown in Figure 12, where the diamonds represent the differences between the corrected CDS values and the predicted linear response versus fractional well depth (for the same pixel as used for Fig. 11) for the 50-exposure run of different illumination exposures. The dot-dashed lines show the envelope of expected rms data differences based only on photometric and read noise contributions. The actual data distribution matches this model quite well, with about half of the data points located within the photometric model envelope and half outside the envelope (versus the 67% expected to be within the envelope). The dashed lines show the envelope of expected rms deviations for linearity corrections accurate only to 1% of the pixel value (e.g., Vacca et al. 2003). The Mimir linearity correction method maintains photometric precision and accuracy to a lower level than 1%, perhaps as good as about 0.3% for single images. The polarimetric data collection methodology for Mimir observations employs multiple images collected at each integration time step, typically 5–20. For 10 such images, the resulting scatter is at or under the 0.1% correction uncertainty required to perform accurate polarimetry.

This nonlinearity correction process is more involved than that presented by Vacca et al. (2003) and requires keeping both first and second reads for all science and calibration CDS

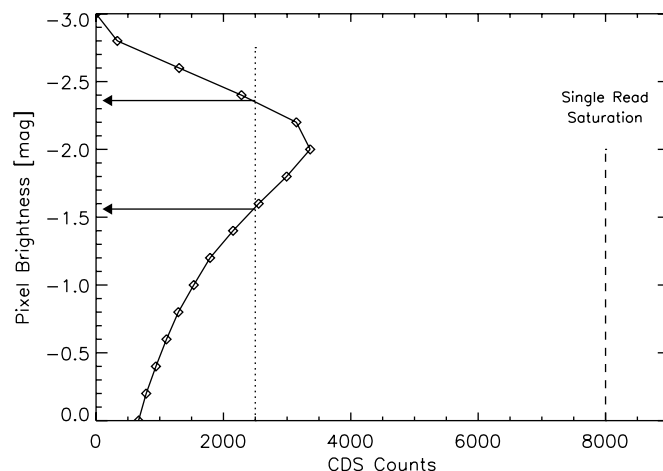


FIG. 13.—Response of a single Mimir pixel (that of Fig. 11) to a range of illumination levels. Horizontal axis is the “classical” CDS counts. Vertical axis is pixel illumination (in magnitudes). Open diamonds, connected by solid line: Classical CDS values obtained for model illuminations stepped by 0.2 mag. Vertical dashed line: Single readout saturation, referenced to reset release (RR). Note that the classical CDS counts never reach this saturation level for this illumination range. The vertical dotted line at left represents a CDS value that an observer might obtain and its two possible illumination values.

images. However, this approach is required to achieve the correction accurate polarimetry demands and is vital to detecting saturated pixels in wide-field images containing vastly different stellar or spectroscopic illuminations, as highlighted in Figure 13. This figure shows the response of 1 pixel in Mimir’s detector to a modeled range of illuminations of that pixel as the illumination levels pass through saturation of the second, then first readout comprising a classical CDS image. The classical CDS counts increase with pixel illumination up to a point, then *decrease* with increasing illumination due to saturation of the pixel after the first readout but before the second. At brighter illuminations, the saturation condition moves earlier to finally affect the first readout, resulting in zero classical CDS counts. Without Mimir’s capability for saving and evaluating *both* readouts that comprise a CDS image, detection of this “early onset” saturation would be almost impossible to detect. From the observer’s standpoint, the effects can be horrible. The vertical dotted line represents a CDS count value an observer might obtain for this pixel. This line intercepts the actual response of the pixel for two different illumination levels, leading to potentially biased or corrupted science data. In summary, capture of *both* images comprising a CDS-type image is required for obtaining reliable scientific data.

### 7.3. Throughput

The optical throughput of Mimir was estimated based on combining the wavelength dependence of transmission through the different lens materials, the filter transmission curves, and the quantum efficiency of the detector. Spectrophotometric

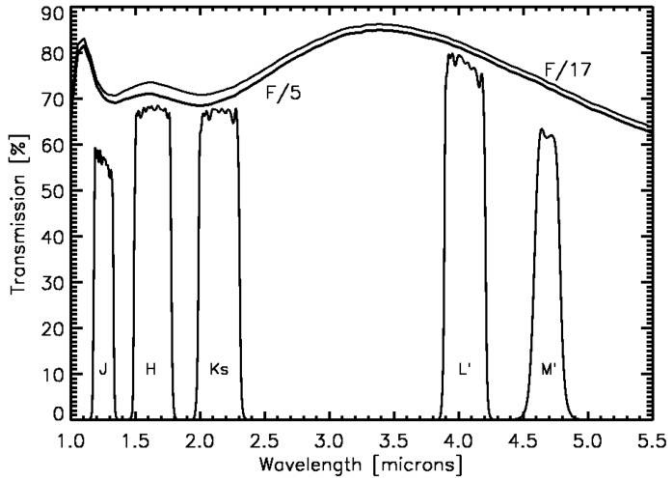


FIG. 14.—Estimated transmission through Mimir optics as a function of wavelength, based on measured spectrophotometry of witness samples of AR-coated LiF, BaF<sub>2</sub>, ZnSe, and ZnS. The upper curve is appropriate to the F/17 camera, the lower, thicker curve for the F/5 camera. Both include the cryostat window and collimator optics. The filter curves are the convolution of the MKO-IR filter set response, as measured by Barr Associates, with the F/5 transmission curve.

transmission curves for each lens material, as measured by Lambda Research Optics for witness samples, were multiplied to model the expected transmission of the entire Mimir optics system, including front window, collimator, and camera(s), resulting in the curves at the top of Figure 14. The total transmission ranges from about 70% to 85%. In the same figure, the expected transmissions including the MKO-NIR filter set are shown, based on spectrophotometric curves measured at 77 K by Barr Associates (Westford, Massachusetts).

The Raytheon detector quantum efficiency estimate is 90%. Combined with telescope optics transmission estimates, this leads to net detection of about 33%–37%, 39%–44%, and 39%–44%, respectively, for *J*-, *H*-, and *K<sub>s</sub>*-band photons. The emissivity of the Perkins Telescope was measured by Mimir to be 29% prior to realuminization in 2007 August and 18% after that. The sensitivity values listed in Table 5 quote *JHK* for the F/5 optics, and *L'* for the F/17 optics and were obtained prior to realuminization.

## 7.4. Imaging

Image quality across both the F/5 and F/17 fields is excellent. The *J*, *H*, and *K<sub>s</sub>* plate scales match each other to much better than 1 pixel, allowing simple registration to produce three-color images. Out to the corners of the image, there are no color shifts indicative of plate scale differences among the bands. At optimal focus, stellar profiles are round across the full 10' × 10' field, showing some coma when off focus. The weak astigmatism present in the Perkins telescope is exploited to perform rapid (~5 s) focusing. PSF sizes in the F/5 mode are generally around 2.5–2.8 pixels FWHM, but during good seeing can go under 2 pixels. The F/17 camera is diffraction-limited and the pixel sizes chosen to exploit subarcsecond seeing.

## 7.5. Spectroscopy

Mimir spectroscopy utilizes gratings and long-pass filters (to suppress order overlap), as well as slit and camera selection, to determine spectral resolution, spectral coverage, and throughput. Grisms currently installed in Mimir consist of CaF<sub>2</sub> prisms with transmission gratings replicated in epoxy on the hypotenuse faces. The “*JHK*” grism (Table 3) covers one octave with a resolving power  $R \sim 500$ –600 (dispersion of 1.4 nm pixel<sup>-1</sup>) at 2 pixel resolution. The two other gratings installed are the “*LM*” grism, for first-order use from 2.8 to 5.5 μm, and the “*SED*” grism, for low resolution on faint objects, primarily across the *JHK* bands.

Wavelength calibration is achieved using OH night sky lines and/or an argon emission lamp. The 5' tall slit put images of the lamp or night sky lines onto approximately 500 detector rows. The dispersion fit consists of a dominant linear component and a weak parabolic term. The values depend weakly on location along the slit; the dependences are included in a 2D dispersion equation fit to the calibration lines. Applying the 2D dependence results in wavelengths corrected to 0.1 pixel (0.14 nm) rms. The action of the fast F/5 camera in conjunction with the grism produces spectra that are sharp and well focused at the center of the array but that broaden along the slit long-axis direction at the wavelength extremes in parabolic fashion. Spectral resolution has a similar weak degradation near the ends of the spectrum.

TABLE 5  
SUMMARY OF MIMIR IMAGING SENSITIVITY

| Band                       | Pixel Size<br>(arcsec) | Zenith Count Rate<br>(ADU s <sup>-1</sup> pixel <sup>-1</sup> ) | Point-Source Sensitivity                       |                            |
|----------------------------|------------------------|---|--|----------------------------|
|                            |                        |   | Zero Point<br>(mag for 1 ADU s <sup>-1</sup> ) | 5 $\sigma$ in 1 h<br>(mag) |
| <i>J</i> .....             | 0.59                   | 19  | 19.4   | 19.1                       |
| <i>H</i> .....             | 0.59                   | 120   | 19.6   | 18.3                       |
| <i>K<sub>s</sub></i> ..... | 0.59                   | 130   | 18.4   | 17.1                       |
| <i>L'</i> .....            | 0.18                   | 64,000  | 18.4   | 12.5                       |

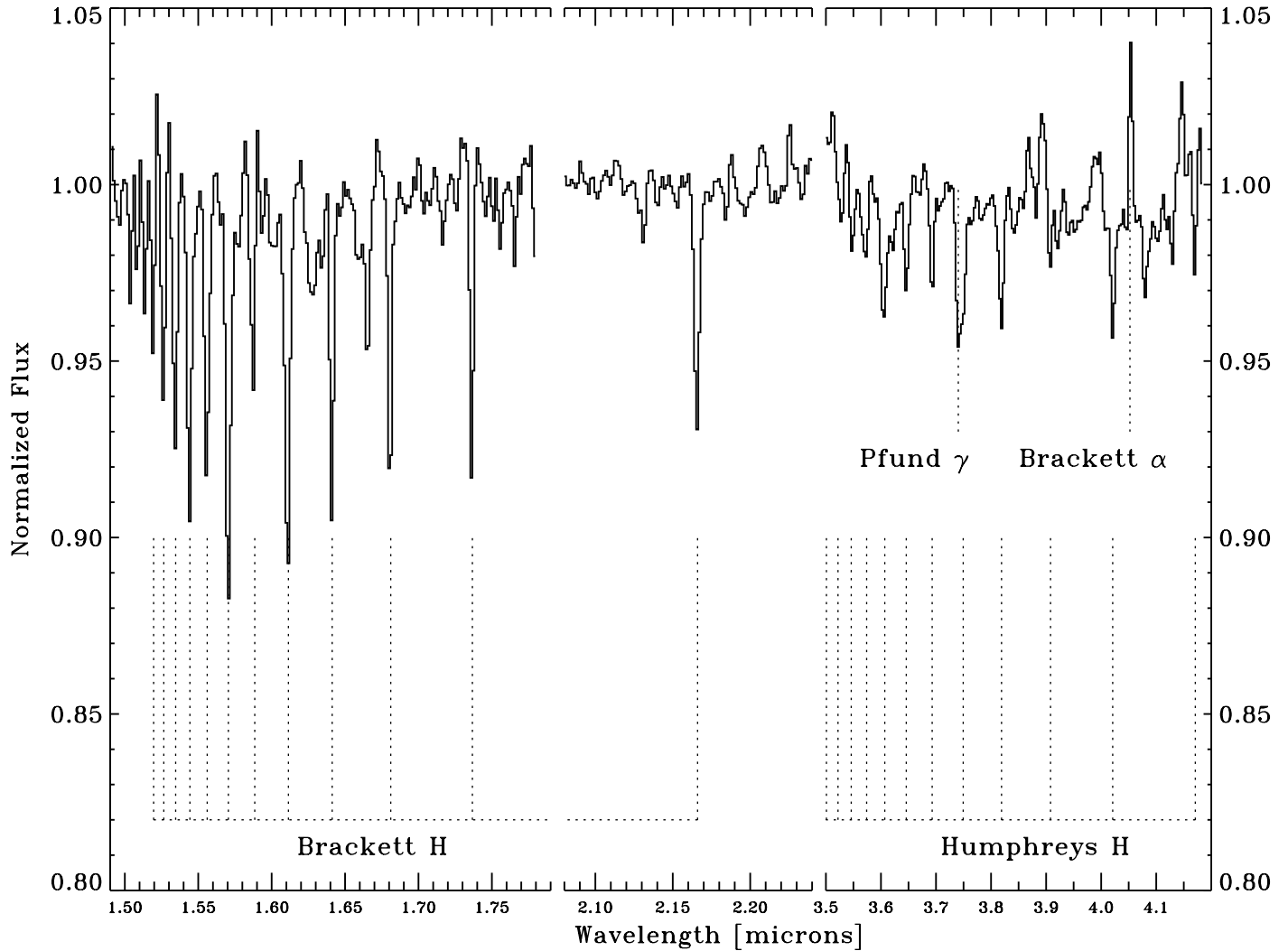


FIG. 15.—Example Mimir spectra obtained toward HD 31964. The  $H$ - and  $K$ -band portions utilized the  $JHK$  grism; the  $L$ -band portion used the  $LM$  grism.

Figure 15 shows example spectra obtained with the  $JHK$  and  $LM$  grisms toward HD 31964. The spectra in the  $H$ ,  $K$ , and  $L$  bands are dominated by hydrogen absorption series plus emission from the Brackett  $\alpha$  line at  $4.05 \mu\text{m}$ . The spectra have been normalized by their continua, corrected for telluric absorption using A0 V stars, and analyzed with the SpeXtool package (Cushing et al. 2004) and custom IDL programs. Spectroscopic efficiency, including slit losses, is about 24%, relative to the system throughput in direct imaging mode, or about 10% overall. Mimir’s spectroscopy mode was optimized for moderate-dispersion high-throughput single slit work, although both lower resolution and higher resolution modes are available. Use of the F/17 camera, when combined with the narrower slits (as small as  $0.36''$  wide—2 pixels for F/17), results in spectral resolutions of 1500–1900 over narrower wavelength bands.

## 7.6. Polarimetry

Polarimetry with Mimir is achieved by combining the actions of the rotatable half-wave plate polarization modulator, band-pass filters, and the wire-grid polarization analyzer. Obtaining polarimetric data consists of taking images, normally a set of 16, through distinct rotational position angles of the HWP. The resulting  $4\theta$  modulation is shown in Figure 16 for a relatively highly polarized (5%) star and a weakly polarized (0.3%) star. The amplitude of the sinusoid is a measure of the degree of polarization (polarization percentage) and the phase offset of the sinusoid relates to the position angle of the linear polarization, as projected onto the plane of the sky.

An estimate of Mimir’s polarimetric efficiency was based on the manufacturer’s characterization of the wire grid efficiency (93%), and the efficiency calculated for the  $H$ -band HWP. This

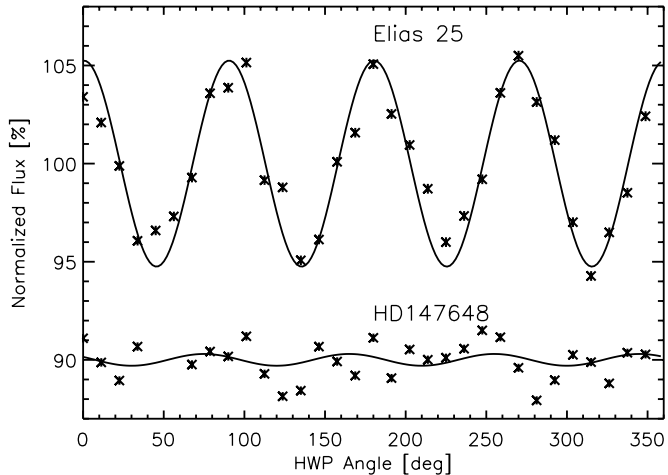


FIG. 16.—Normalized flux vs. half-wave plate rotation angle for a highly polarized standard star (Elias 25;  $\sim 5\%$ ) and a weakly polarized standard (HD 147648;  $\sim 0.3\%$ ) showing four cycle modulation. Crosses indicate Mimir measured data points; sinusoid curves are fits.

HWP consists of two roughly 1 mm thick  $\text{MgF}_2$  plates, with optical axes rotated  $90^\circ$ . Based on the angles of light leaving and entering the HWP, we expected its polarimetric efficiency to be 97.8%. When combined with the wire grid efficiency, Mimir ought to show about 90.9% efficiency when measuring polarization.

We used Mimir polarimetric observations of 15 stars from the Whittet et al. (1992) list and selected to span 0%–4% polarization and all polarization position angles. Figure 17 shows a comparison of Mimir-measured polarizations for these stars versus their Whittet et al. values. To achieve these comparisons, all raw Mimir polarizations were analyzed to yield instrumental Stokes  $U$  and  $Q$  values and were tagged to the position of the star in the Mimir field of view (FOV). Most of the 15 stars were placed near the FOV center for their observations. However, for one grouping of three standard stars that appeared simultaneously in the FOV, we performed a  $5 \times 5$  raster grid of observations across the Mimir FOV. From knowledge of the “standard” polarization properties of each stars, we derived their sky-based Stokes  $U$  and  $Q$  values.

Multiple parameter regressions were performed to fit the instrumentally measured Stokes parameters to the sky Stokes parameters to determine the instrumental polarization properties. The best fits were obtained when the polarization efficiency and instrument offset angle did not vary across the FOV but the instrumental polarization and its position angle were allowed to vary parabolically. Figure 18 displays a contour representation of the derived instrumental polarization across the FOV and shows where on the FOV the standard star observations took place. The minimum instrumental polarization is under 0.2% at the FOV center and grows to nearly 4% at the corners. However, the high density of sample points near (600, 400) may be

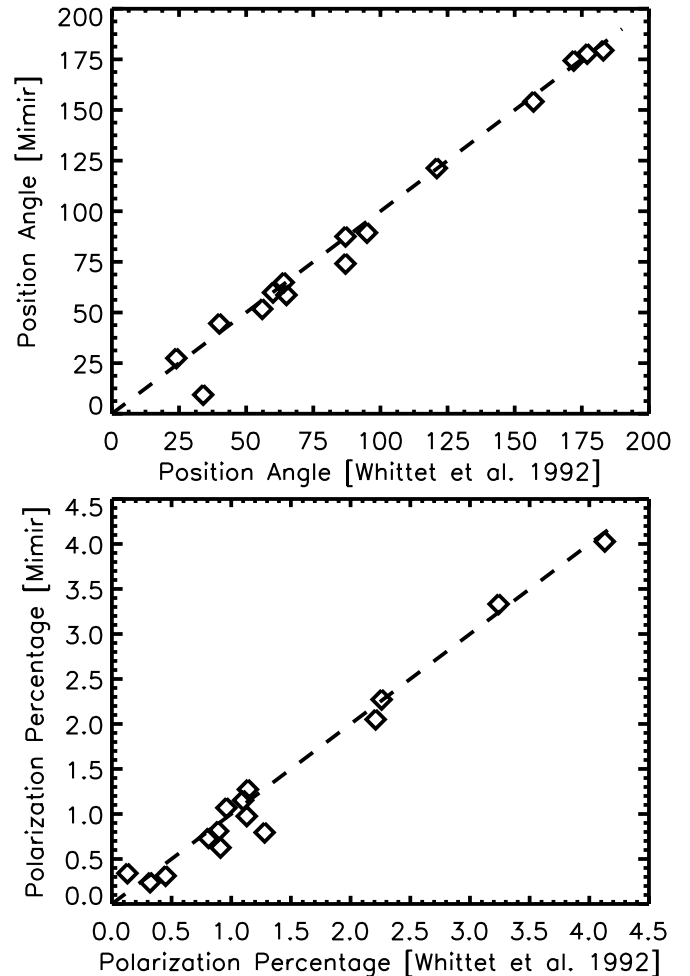


FIG. 17.—Comparison of Mimir measured vs. published (Whittet et al. 1992) linear polarization properties for 15 standard stars. *Upper panel:* Comparison of polarization position angles, measured in degrees toward east from north on the sky. Dashed line has unit slope and zero offset. *Bottom panel:* Comparison of polarization percentage values.

overweighting central measurements at the expense of the few measurements near the field corners, so remeasurement with better corner sampling might be expected to yield a less pronounced increase into the corners. The best fit obtained from analysis

of these data yields an instrument polarization efficiency of  $91.2\% \pm 2.5\%$ , in good agreement with the expected value of 90.9%.

The chief goal for Mimir polarimetry is to survey vast areas of the northern Milky Way’s disk to map the Galactic magnetic field. A short pilot study of two regions was conducted in 2005 May and June to establish survey parameters and expected performances. Figure 19 shows the run of polarimetric uncertainty derived from Mimir polarimetric observations versus stellar magnitude for short, 3 s duration observations at each of 32 HWP position angles. The plot shows that significant linear

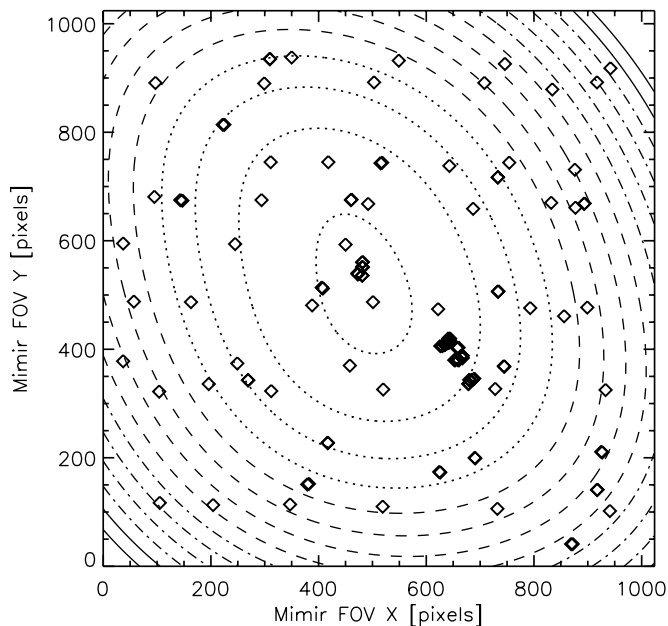


FIG. 18.—Contour representation of derived instrumental polarization percentage, mapped across the field of view. Contours begin at 0.2% near the field center and increase by 0.1% outward. Diamonds identify locations on the detector array of standard star polarization measurements. Note dense clump below and to the right of the field center.

polarization (with  $S/N > 3$ ) can be measured for most stars brighter than 12 mag in  $H$  band.

Figure 20 shows a composite image of one of the 42 FOVs making up the pilot polarization survey. The background gray-

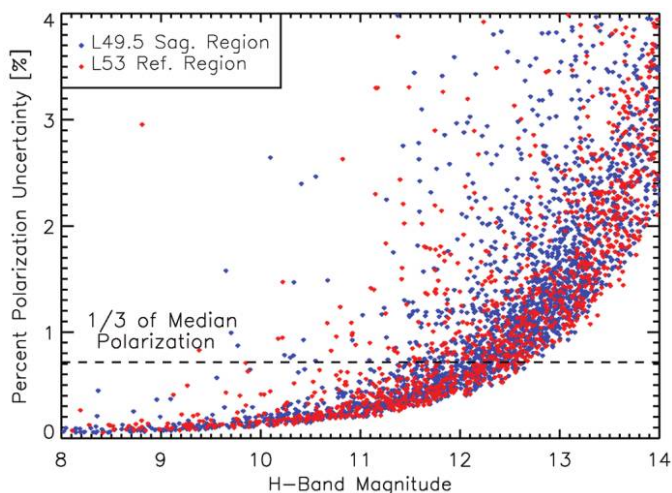


FIG. 19.—Polarization uncertainty vs.  $H$ -band photometric magnitude, for stars observed by Mimir toward two Galactic plane test regions (Galactic longitudes  $L = 53$  and  $L = 49.5$ ). Horizontal dashed line shows the value of polarimetric uncertainty corresponding to one-third of the mean polarization value seen toward these two fields, showing that useful polarizations were obtained for these short observations down to  $H \sim 12$ .

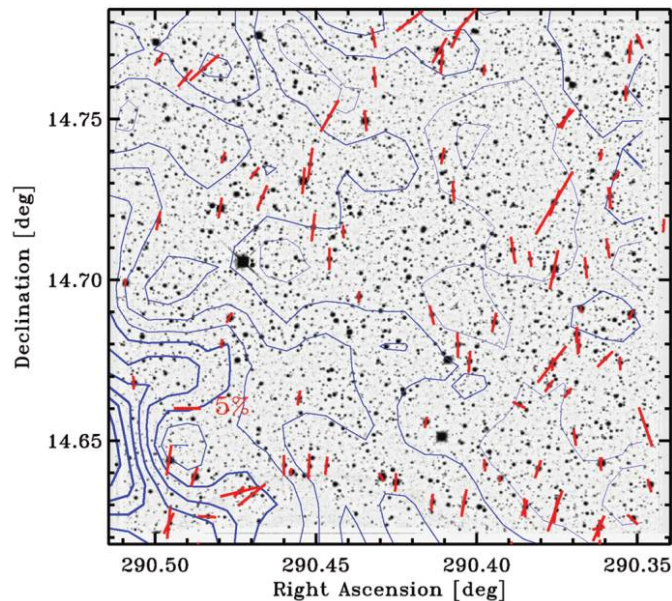


FIG. 20.—Deep Mimir  $H$ -band image (gray scale) overlaid with (blue) contours of  $^{13}\text{CO}$  emission from the GRS and (red) linear polarization vectors from the Mimir pilot survey, for a single  $10' \times 10'$  field toward  $L = 49.5$ . A 5% reference vector is shown. The image shows stars brighter than about 17 mag at  $H$  band.

scale image was formed from the addition of all  $H$ -band images and reaches to  $H = 16$ – $17$  mag, some 1–2 mag fainter than the 2MASS point-source catalog listings for this field. The blue contours represent the distribution of molecular hydrogen gas, as traced by the  $^{13}\text{CO}$  molecule and mapped by the Galactic Ring Survey (Jackson et al. 2006). The red vectors represent the linear polarizations measured by Mimir for the stars brighter than  $H = 12$  mag in this field and trace the direction of the magnetic field, as projected onto the plane of the sky. The large field of view of Mimir in this polarimetric mode yields a tremendous multiplex advantage, enabling surveying large numbers of distant stars for foreground magnetic fields in a relatively short time.

## 8. SUMMARY

In response to wide ranging scientific needs, the Mimir instrument was designed as a multifunction tool for imaging, polarimetry, and low-to-moderate resolution spectroscopy across the entire 1– $5 \mu\text{m}$  wavelength range. Mimir features all refractive optics, a reimaging design, and a “facility-class” operations approach that has resulted in an instrument capable of delivering reliable images and spectra for many years to come.

The wide  $10' \times 10'$  field, four filter wheels, and rapid mode changes between imaging, spectroscopy, and polarimetry make Mimir an exceedingly versatile instrument. The wide-field plate scale of  $0.59'' \text{ pixel}^{-1}$  onto the ALADDIN III  $1024 \times 1024$  detector array is well matched to the median NIR seeing at the Perkins Telescope. The narrow-field plate scale of  $0.18''$

pixel<sup>-1</sup> is ideal for higher resolution *JHK* projects and for long-wavelength (*L'* and *M'*) imaging. Imaging polarimetry in the NIR over the full 10' wide field is a capability unique to Mimir. Rapid mode changes allow switching to spectroscopic observing to respond to changing weather conditions or to combine with direct imaging for time-resolved spectrophotometric projects.

Three years of operations experience of Mimir on the Perkins telescope has resulted in smoother and improved operations, reduced system overheads, and a large number of user programs obtaining high quality data. We expect the useful lifetime for Mimir on the Perkins to exceed a decade or more and to produce excellent science across a wide span of topics and studies.

The Mimir team is deeply indebted to its financial sponsors, many vendors and services providers, and to the faculty, scientists, and students who have helped move us forward. Our external sponsors were NASA (grants NAG5-8716 and NAG5-9578), NSF (AST 99-87335 and 06-07500), and the W. M. Keck Foundation. D. C. gratefully acknowledges CY2002 sabbatical support from Boston University. The Boston University Scientific Instrument Facility fabricated nearly all of the more than 1500 individual parts comprising Mimir. Mimir's optics were fabricated by Lambda Research Optics (Costa Mesa, California). At Lowell Observatory, Mimir has been aided during both repairs and operations by the superb technical staff.

## REFERENCES

- Cushing, M. C., Vacca, W. D., & Rayner, J. T. 2004, *PASP*, 116, 362  
 Depoy, D. L., Atwood, B., Byard, P. L., Frogel, J., & O'Brien, T. P. 1993, *Proc. SPIE*, 1946, 667  
 Elston, R. 1998, *Proc. SPIE*, 3354, 404  
 Feldman, A., Horowitz, D., Waxler, R. M., & Dodge, M. J. 1979, NBS Rep. TN993  
 Greene, T. P., Tokunaga, A. T., Toomey, D. W., & Carr, J. S. 1993, *Proc. SPIE*, 1946, 313  
 Grundy, W. M., & Buie, M. W. 2000a, *AAS/DPS*, 32, 45.06; *BAAS*, 32, 1083  
 ———. 2002, *Icarus*, 157, 128  
 Grundy, W. M., Buie, M. W., Spencer, J. R., Young, L. A., & Young, E. F. 2003, *BAAS*, 35, 957  
 Hinkle, K. H., Cuberly, R. W., Gaughan, N. A., Heynssens, J. B., Joyce, R. R., Ridgway, S. T., Schmitt, P., & Simmons, J. E. 1998, *Proc. SPIE*, 3354, 810  
 Hodapp, K. W. et al. 2003, *PASP*, 115, 1388  
 Horn, J. M., & McLean, I. S. 2000, *Proc. SPIE*, 4008, 979  
 Horn, J. M. et al. 2000, *Proc. SPIE*, 4014, 65  
 Jackson, J. M. et al. 2006, *ApJS*, 163, 145  
 McLean, I. S. et al. 1998, *Proc. SPIE*, 3354, 566  
 Rayner, J. T., Toomey, D. W., Onaka, P. M., Denault, A. J., Stahlberger, W. E., Vacca, W. D., & Cushing, M. C. 2003, *PASP*, 115, 362  
 Shure, M. A., Toomey, D. W., Rayner, J. T., Onaka, P. M., & Denault, A. J. 1994, *Proc. SPIE*, 2198, 614  
 Simons, D. A., & Tokunaga, A. 2002, *PASP*, 114, 169  
 Taylor, B. W., Dunham, E. W., & Elliot, J. L. 2004, *Proc. SPIE*, 5496, 446  
 Taylor, B. W., Dunham, E. W., Gould, A. J., Osip, D. J., & Elliot, J. L. 2000, *Proc. SPIE*, 4009, 449  
 Tokunaga, A. T., Simons, D. A., & Vacca, W. D. 2002, *PASP*, 114, 180  
 Tokunaga, A. T., & Vacca, W. D. 2005, *PASP*, 117, 421  
 Tollestrup, E. V., & Willner, S. P. 1998, *Proc. SPIE*, 3354, 502  
 Vacca, W. D., Cushing, M. C., & Rayner, J. T. 2003, *PASP*, 115, 389  
 Whittet, D. C. B., Martin, P. G., Hough, J. H., Rouse, M. F., Bailey, J. A., & Axon, D. J. 1992, *ApJ*, 386, 562  
 Yoder, P. R., Jr. 1995, *Mounting Lenses in Optical Instruments*, (Bellingham: SPIE)